Quantitative formulation of frequency-dependent interaction force for practical applications in amplitude-modulation atomic force microscopy

Kenichi Umeda,[1,2,*] Karen Kamoshita,[3] and Noriyuki Kodera[1,†]

[1] *Nano Life Science Institute (WPI-NanoLSI), Kanazawa University, Kakuma-machi, Kanazawa, Ishikawa, 920-1192, Japan*

[2] *PRESTO/JST, 4-1-8 Honcho, Kawaguchi, Saitama 332-0012, Japan*

[3] *School of Mathematics and Physics, College of Science and Engineering, Kanazawa University, Kakuma-machi, Kanazawa, Ishikawa, 920-1192, Japan*

(Received 26 November 2024; revised 5 February 2025; accepted 18 February 2025; published 25 March 2025)

Amplitude-modulation atomic force microscopy (AM-AFM) measures nanoscale surface structures by detecting changes in the cantilever oscillation amplitude, contributing to materials research. AM-AFM can nondestructively observe fragile molecules, such as biomolecules, even while the probe is in intermittent contact with the sample. However, the interaction force estimated from experimental amplitude values is significantly greater than actual molecular binding forces, despite the successful visualization of molecular dynamics, raising a fundamental question about force quantification. Here, we formulate a quantitative force conversion equation for arbitrary driving frequencies. A comprehensive theoretical analysis reveals that, when the cantilever is excited at the resonance slope, the conventional equation overestimates the actual force by approximately five times since it is valid only for excitation at the resonance frequency. This mathematical framework is validated through simulations and experiments, offering new insights into AM-AFM force estimation. The findings provide a crucial toolset for accurate yet easy-to-use force quantification, enhancing the reliability of practical AM-AFM applications in materials and biomolecular research.

DOI: 10.1103/PhysRevApplied.23.034065

I. INTRODUCTION

Amplitude-modulation (tapping-mode) atomic force microscopy (AM-AFM) is a dynamic-mode AFM technique that enables high-resolution imaging at the atomic and molecular scale with minimal perturbation [1–3]. It has been employed in various materials science research areas, e.g., electrochemistry [4], electronics [5–7], physicochemistry [8], and polymers [5,6,9,10], since it operates effectively in liquid as well as ambient environments. Notably, this technique has contributed to the visualization of living biological samples at the nanoscale [2,5,11–14]. Recent advancements in the bandwidth of AM-AFM devices have facilitated the development of high-speed AFM (HS-AFM), which has uncovered the submolecular-scale dynamics of biomolecules [12,15–21].

A unique feature of AFM is that the tip–sample interaction force can serve not only as a feedback signal but also as a force sensor or stimulator. In bio-applications, it has been employed for the mechanical investigations of force-sensing ion channels [12] or antibody conjugates [22], and for the manipulation or disassembly of supramolecular complexes [11,13,16–18]. Therefore, quantitative estimation of the tip–sample force is essential for gaining deeper insight into their mechanical properties and contributes to optimizing feedback parameters required for nondestructive imaging of fragile molecules.

There are two primary ways to quantify the forces detected by the AFM tip: the average force and the peak force [23,24]. Despite the fact that estimating peak force is extremely challenging both experimentally and theoretically, it is considered important for biomolecular disruption [22,24] and for evaluating the viscoelastic, chemical, and electronic properties of the sample surface [8,25,26]. As a result, quantitative force volume mapping [8,10,27–29] and other novel methods [18,22–24,26,30,31] have been proposed.

In contrast to the estimation of the peak force, which requires time-consuming experiments, the average force can be more easily estimated from the amplitude setpoint value, making it more suitable for the practical imaging of fragile biomolecules in action. In 2001, San Paulo et al. derived an approximate equation for estimating average force from amplitude values [32,33], which remains widely used in AFM studies to this day [9,12,14,15,17].

---

[*] Contact author: umeda.k@staff.kanazawa-u.ac.jp

[†] Contact author: nkodera@staff.kanazawa-u.ac.jp

However, as discussed later, using this formula typically estimates the average force to be several tens of piconewtons under typical HS-AFM experimental conditions. In contrast, actual HS-AFM experiments have enabled the observation of bioconjugates with equilibrium binding forces as small as a few piconewtons [34,35]. If such fragile molecules were subjected to forces of tens of piconewtons, their structure and dynamics would likely be disrupted.

Moreover, since the peak force is typically one order of magnitude greater than the average force [23,24], the peak force estimated from the amplitude value can reach hundreds of piconewtons. In contrast, a method has also been proposed to estimate the peak force during topographic imaging by referring to a separately obtained force curve [22]. According to this method, the peak force can be reduced to several tens of piconewtons in nondestructive bio-imaging applications. These discrepancies raise the question of why the forces derived from amplitude values are an order of magnitude larger than biological binding forces and even those commonly encountered in bio-imaging.

Additionally, the equation by San Paulo et al. does not account for excitation frequency dependence, even though AM-AFM experiments are often performed with excitation slightly off-resonance. Although some studies have explored the effects of excitation frequency on force estimation [1,24,36–38], their findings have been limited in scope, and a comprehensive theoretical framework with experimental and simulation-based validation has yet to be established.

In this study, we derive a quantitative conversion equation to estimate the average force from the amplitude values at arbitrary drive frequencies. Our comprehensive theoretical analysis reveals that the estimated average force depends strongly on the driving frequency and can be up to five times smaller when excited at the resonance slope rather than at the resonance frequency (f_0). This finding resolves a longstanding issue in AM-AFM force estimation and provides a theoretical framework that integrates with the widely used conventional approximated equation. It also extends to the estimation of peak forces, offering more accurate results while maintaining ease of use.

II. CONVERSION OF AMPLITUDE TO AVERAGE FORCE

In AM-AFM, to observe fragile biomolecules without destroying them, it is generally recognized that driving the cantilever at the resonance slope is essential to achieve maximum force sensitivity [1]. However, most previous studies have focused on the excitation at f_0. Therefore, in this section, we derive a theoretical equation for the average force that can be applied to an arbitrary driving frequency (f_{drive}).

The equation of motion of the cantilever based on a simple harmonic oscillator model is expressed as follows:

$$\begin{aligned}\frac{k_{\mathrm{cl}}}{\omega_0^2} z''_{\mathrm{tip}}(t) &+ \frac{k_{\mathrm{cl}}}{\omega_0 Q_{\mathrm{cl}}} z'_{\mathrm{tip}}(t) + k_{\mathrm{cl}} z_{\mathrm{tip}}(t) \\ &= \underbrace{F_{\mathrm{drive}} \cos(\omega_{\mathrm{drive}} t)}_{\text{External driving force}} + \underbrace{F_{\mathrm{ts}}(z_{\mathrm{tip}}(t), z'_{\mathrm{tip}}(t))}_{\text{Tip-sample force}}, \end{aligned} \tag{1}$$

where ω_0 ($=2\pi f_0$), Q_{cl}, k_{cl}, F_{drive}, ω_{drive} ($=2\pi f_{\mathrm{drive}}$), and z_{tip} are the eigenfrequency, quality factor, spring constant, driving force, driving frequency, and displacement of the cantilever, respectively. Hereafter, we denote f and ω ($=2\pi f$) as a certain frequency and its angular frequency, respectively.

Normally, the distance dependence of the tip–sample interaction is nonlinear; however, when the interaction depth is relatively small, the harmonic components can be ignored. Assuming a steady-state oscillation, z_{tip} can be approximately expressed as

$$z_{\mathrm{tip}}(t) \approx \langle z_{\mathrm{tip}} \rangle + A_{\mathrm{cl}} \cos(\omega_{\mathrm{drive}} t + \phi_{\mathrm{cl}}), \tag{2}$$

where A_{cl} and ϕ_{cl} are the oscillation amplitude and phase delay in the excitation system, respectively. Using the Fourier series of the tip–sample interaction, we solve this equation to obtain the transfer function G_{cl} as follows [29]:

$$G_{\mathrm{cl}}(\tilde{\omega}_{\mathrm{drive}}) = \frac{1}{k_{\mathrm{cl}}} \frac{1}{(1 - \tilde{\omega}_{\mathrm{drive}}^2 - I_{\mathrm{even}}(z_{\mathrm{tip}}, A_{\mathrm{cl}})) + i(\tilde{\omega}_{\mathrm{drive}}/Q_{\mathrm{cl}} + I_{\mathrm{odd}}(z_{\mathrm{tip}}, A_{\mathrm{cl}}))}, \tag{3}$$

where $\tilde{\omega}_{\mathrm{drive}}$ is a normalized f_{drive} that is defined as follows:

$$\tilde{\omega}_{\mathrm{drive}} \equiv \frac{\omega_{\mathrm{drive}}}{\omega_0} = \frac{f_{\mathrm{drive}}}{f_0}, \tag{4}$$

and I_{even} and I_{odd} represent the in-phase and out-of-phase terms of the Fourier components, reflecting conservative forces and energy dissipation, respectively [29], and are expressed as

$$\begin{aligned} I_{\mathrm{even}}(z_{\mathrm{tip}}, A_{\mathrm{cl}}) &= \frac{2f_{\mathrm{drive}}}{k_{\mathrm{cl}}A_{\mathrm{cl}}} \int_0^{1/f_{\mathrm{drive}}} F_{\mathrm{ts}}(z_{\mathrm{tip}}(t), z'_{\mathrm{tip}}(t)) \cos(\omega_{\mathrm{drive}}t + \phi_{\mathrm{drive}})\mathrm{d}t \\ &= \frac{2}{k_{\mathrm{cl}}A_{\mathrm{cl}}^2} \left\langle F_{\mathrm{ts}} z_{\mathrm{tip}} \right\rangle \propto \Delta f\,, \end{aligned} \tag{5}$$

$$\begin{aligned} I_{\mathrm{odd}}(z_{\mathrm{tip}}, A_{\mathrm{cl}}) &= \frac{2f_{\mathrm{drive}}}{k_{\mathrm{cl}}A_{\mathrm{cl}}} \int_0^{1/f_{\mathrm{drive}}} F_{\mathrm{ts}}(z_{\mathrm{tip}}(t), z'_{\mathrm{tip}}(t)) \sin(\omega_{\mathrm{drive}}t + \phi_{\mathrm{drive}})\mathrm{d}t \\ &= -\frac{1}{\pi f_{\mathrm{drive}} k_{\mathrm{cl}}A_{\mathrm{cl}}^2} \left\langle F_{\mathrm{ts}} z'_{\mathrm{tip}} \right\rangle, \end{aligned} \tag{6}$$

where F_{ts} is the tip–sample interaction force. By following the original definition by Dürig et al. [39], we define them as even or odd relative to the tip trajectory. Moreover, A_{cl} and ϕ_{cl} are calculated as follows:

$$\begin{aligned} A_{\mathrm{cl}}(\tilde{\omega}_{\mathrm{drive}}) &= |G_{\mathrm{cl}}(\tilde{\omega}_{\mathrm{drive}})|F_{\mathrm{drive}} \\ &= \frac{A_0}{\sqrt{(1-\tilde{\omega}_{\mathrm{drive}}^2 - I_{\mathrm{even}}(z_{\mathrm{tip}}, A_{\mathrm{cl}}))^2 + (\tilde{\omega}_{\mathrm{drive}}/Q_{\mathrm{cl}} + I_{\mathrm{odd}}(z_{\mathrm{tip}}, A_{\mathrm{cl}}))^2}}, \end{aligned} \tag{7}$$

$$\phi_{\mathrm{cl}}(\tilde{\omega}_{\mathrm{drive}}) = \angle G_{\mathrm{cl}}(\tilde{\omega}_{\mathrm{drive}}) = \tan^{-1}\left(-\frac{\tilde{\omega}_{\mathrm{drive}}/Q_{\mathrm{cl}} + I_{\mathrm{odd}}(z_{\mathrm{tip}}, A_{\mathrm{cl}})}{1-\tilde{\omega}_{\mathrm{drive}}^2 - I_{\mathrm{even}}(z_{\mathrm{tip}}, A_{\mathrm{cl}})}\right), \tag{8}$$

respectively, where A_0 represents A_{cl} at $\tilde{\omega}_{\mathrm{drive}} = 0$. When $F_{\mathrm{ts}}=0$, A_{cl} is expressed by

$$A_{\mathrm{cl}}(\tilde{\omega}_{\mathrm{drive}}, I_{\mathrm{even}} = I_{\mathrm{odd}} = 0) = \frac{A_0}{\sqrt{(1-\tilde{\omega}_{\mathrm{drive}}^2)^2 + (\tilde{\omega}_{\mathrm{drive}}/Q_{\mathrm{cl}})^2}}. \tag{9}$$

The frequency characteristics of amplitude as a function of I_{even} are analyzed in Fig. 1(a). As the repulsive force is increased ($I_{\mathrm{even}} < 0$), a positive f_0 shift and a reduction in the overall excitation efficiency are observed, which can be attributed to an increase in the effective k_{cl}. In addition, the resonance peak becomes slightly sharper, meaning that the effective Q_{cl} increases, which makes the amplitude change at the resonance peak less sensitive to the force. In contrast, as the attractive force is increased ($I_{\mathrm{even}} > 0$), a negative frequency shift and an increase in the overall excitation efficiency are observed due to the reduction of the effective k_{cl}.

Moreover, the frequency characteristics of amplitude as a function of I_{odd} are analyzed in Fig. 1(b). As I_{odd} increases, Q_{cl} and the overall excitation efficiency decrease, but the f_0 shift is not observed. In other words, the maximum sensitivity for I_{odd} can be obtained by exciting at a frequency close to the resonance peak (a more detailed analysis of dissipation will be published elsewhere).

Enlarged views of the frequency characteristics near the resonance are shown in Figs. 1(c) and 1(d). It is well-known that when Q_{cl} is sufficiently large, the amplitude gain peak appears exactly at f_0. However, as seen here, when Q_{cl} becomes significantly low, the resonance peak frequency (f_{peak}) deviates slightly negatively from f_0. The analytical solution for f_{peak} can be derived by setting the derivative of A_{cl} in Eq. (9) to zero, i.e.,

$$\frac{\partial A_{\mathrm{cl}}(\tilde{\omega}_{\mathrm{drive}})}{\partial \tilde{\omega}_{\mathrm{drive}}} = A_0 \frac{\tilde{\omega}_{\mathrm{drive}}[2(1-\tilde{\omega}_{\mathrm{drive}}^2) - 1/Q_{\mathrm{cl}}^2]}{[(1-\tilde{\omega}_{\mathrm{drive}}^2)^2 + (\tilde{\omega}_{\mathrm{drive}}/Q_{\mathrm{cl}})^2]^{3/2}} = 0. \tag{10}$$

Solving this equation, we obtain the expression of normalized f_{peak} ($\tilde{\omega}_{\mathrm{peak}}$) as follows:

$$\tilde{\omega}_{\mathrm{peak}} \equiv \frac{\omega_{\mathrm{peak}}}{\omega_0} = \frac{f_{\mathrm{peak}}}{f_0} = \sqrt{1 - \frac{1}{2Q_{\mathrm{cl}}^2}} \quad \left(Q_{\mathrm{cl}} > \frac{1}{\sqrt{2}}\right). \tag{11}$$

In Fig 1(c), when excited at f_{peak} or lower, the amplitude value tends to effectively decrease with reducing I_{even}. However, even when I_{even} is changed, the amplitude value is almost unchanged at f_0 and rather increases at a frequency higher than f_0. In contrast, in Fig. 1(d), as I_{odd} is changed, the amplitude value decreases regardless of f_{drive}, especially near f_{peak}.

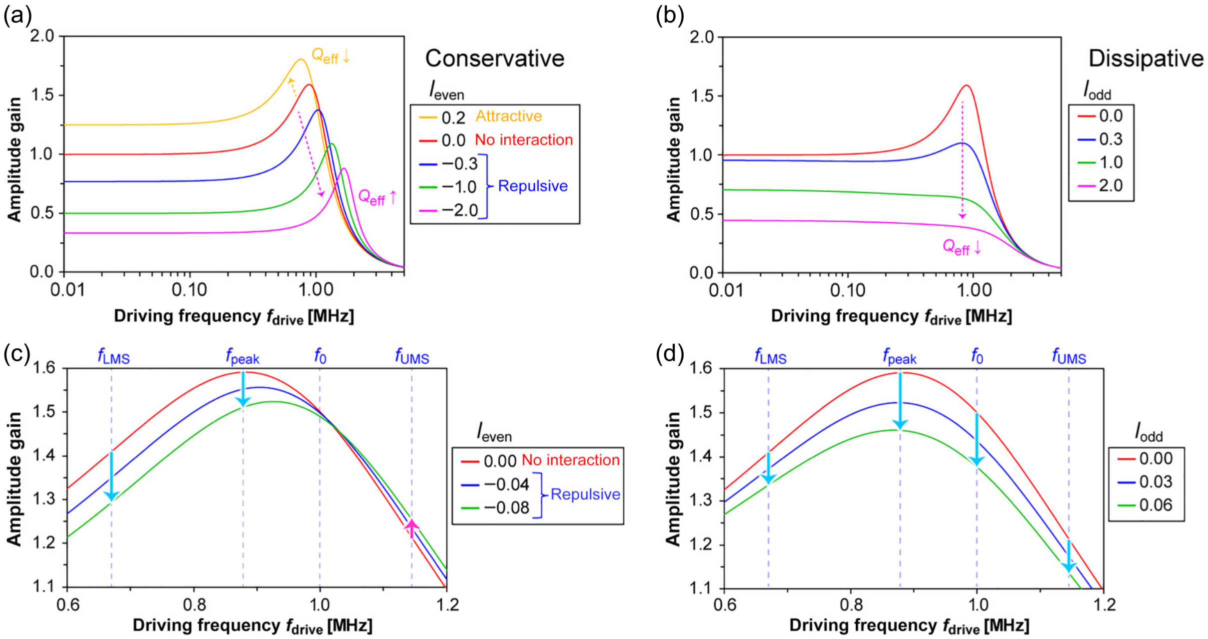

FIG. 1. (a),(b) Theoretical resonance characteristics of the amplitude gain dependent on (a) I_{even} and (b) I_{odd}. Positive and negative signs of I_{even} correspond to the attractive and repulsive forces, respectively. (c),(d) Enlarged views of the resonance amplitude gain dependent on (c) I_{even} and (d) I_{odd}. The vertical broken lines indicate the amplitude variation at several characteristic frequencies, i.e., $f_{\mathrm{LMS}}, f_{\mathrm{peak}}, f_0$, and f_{UMS}, which represent the lower MaxSlope, peak, resonance, and upper MaxSlope frequencies, with the values of 0.67, 0.88, 1, and 1.14 MHz, respectively. All the data are calculated with $Q_{\mathrm{cl}} = 1.5$, a typical value for HS-AFM experiments.

As AM-AFM is also known as the slope detection method [1,3,40], it has been theoretically clarified that the sensitivity of conservative forces, which are reflected in the f_0 shift, is also maximized when the cantilever is excited at the MaxSlope frequency (f_{MS}) at which the amplitude slope is at its maximum. Under ambient conditions [7], the upper MaxSlope frequency [f_{UMS} in Figs. 1(c) and 1(d)] is typically excited to effectively detect the negative frequency shift resulting from attractive interactions whereas, in liquid environments, the lower MaxSlope frequency [f_{LMS} in Figs. 1(c) and 1(d)] is excited to effectively detect the positive frequency shift resulting from repulsive interactions. If the attractive and repulsive forces are switched during imaging, the amplitude will not decrease monotonically as the tip approaches, leading to unstable imaging [29,41,42]. Particularly in liquids, excitation at a slightly lower off-resonance frequency is important not only to improve the sensitivity, but also to compensate for the slight negative shift of f_0 caused by the squeeze film effect during approach [43]. For these reasons, excitation at the slightly off-resonance frequency is typically recommended in most AM-AFM operation manuals [44–48].

In HS-AFM experiments, most protein surfaces are relatively elastic and imaging is performed with the minimum force required; therefore, I_{odd} can be negligible compared with I_{even}. Furthermore, in Eq. (7), by using the free oscillation amplitude (A_{free}), A_{cl} can be expressed as follows:

$$A_{\mathrm{cl}}(\tilde{\omega}_{\mathrm{drive}}) = A_{\mathrm{free}} \sqrt{\frac{\left(1-\tilde{\omega}_{\mathrm{drive}}^2\right)^2 + (\tilde{\omega}_{\mathrm{drive}}/Q_{\mathrm{cl}})^2}{\left(1-\tilde{\omega}_{\mathrm{drive}}^2 - \frac{2}{k_{\mathrm{cl}}A_{\mathrm{cl}}^2}\left\langle F_{\mathrm{ts}} z_{\mathrm{tip}}\right\rangle\right)^2 + (\tilde{\omega}_{\mathrm{drive}}/Q_{\mathrm{cl}})^2}}. \quad (12)$$

This equation is an implicit function of A_{cl} because A_{cl} appears on both sides. When the oscillation amplitude is sufficiently large, such that the tip is in contact with the sample for only a short time during a cantilever period, the large-amplitude approximation can be applied as follows [41]:

$$\lim_{A_{\mathrm{free}}\to\infty} \left\langle F_{\mathrm{ts}} z_{\mathrm{tip}}\right\rangle \approx -A_{\mathrm{cl}} \left\langle F_{\mathrm{ts}}\right\rangle . \quad (13)$$

By solving Eq. (12) for $\langle F_{\mathrm{ts}}\rangle$, we obtain the force conversion equation at arbitrary f_{drive} as follows:

$$\langle F_{\mathrm{ts}}\rangle = \frac{k_{\mathrm{cl}}A_{\mathrm{free}}}{2}\left[-(1-\tilde{\omega}_{\mathrm{drive}}^2)\tilde{A}_{\mathrm{cl}} \overset{\mathrm{rep}}{\underset{\mathrm{att}}{\pm}} \sqrt{\left(1-\tilde{\omega}_{\mathrm{drive}}^2\right)^2 + (\tilde{\omega}_{\mathrm{drive}}/Q_{\mathrm{cl}})^2(1-\tilde{A}_{\mathrm{cl}}^2)}\right], \quad (14)$$

where the positive and negative signs are used for the repulsive ($\langle F_{\mathrm{ts}}\rangle > 0$) and attractive ($\langle F_{\mathrm{ts}}\rangle < 0$) regimes, respectively, and $\tilde{A}_{\mathrm{cl}}$ is a normalized amplitude that is defined as follows:

$$\tilde{A}_{\rm cl} \equiv \frac{A_{\rm cl}}{A_{\rm free}} = \frac{A_{\rm free} + \Delta A_{\rm ts}}{A_{\rm free}}, \tag{15}$$

where $\Delta A_{\rm ts}$ is the amplitude change resulting from the tip–sample interaction. When the feedback error is neglected, $\tilde{A}_{\rm cl}$ represents the setpoint ratio. By substituting ω_0 with $\omega_{\rm drive}$, namely, $\tilde{\omega}_{\rm drive} = 1$, we obtain a well-known conventional conversion equation as follows [9,12,15,17,33]:

$$\langle F_{\rm ts}\rangle = \frac{k_{\rm cl}}{2Q_{\rm cl}}\sqrt{A_{\rm free}^2 - A_{\rm cl}^2} = \frac{k_{\rm cl}A_{\rm free}}{2Q_{\rm cl}}\sqrt{1-\tilde{A}_{\rm cl}}. \tag{16}$$

Conversely, the equation for calculating $A_{\rm cl}$ from $\langle F_{\rm ts}\rangle$ is obtained by solving Eq. (12) for $A_{\rm cl}$ as follows:

$$A_{\rm cl}(\tilde{\omega}_{\rm drive}) = \sqrt{A_{\rm free}^2 - (\tilde{\omega}_{\rm drive}/Q_{\rm cl})^2\beta^2} - (1-\tilde{\omega}_{\rm drive}^2)\beta, \tag{17}$$

where

$$\beta = \frac{2}{[(1-\tilde{\omega}_{\rm drive}^2)^2 + (\tilde{\omega}_{\rm drive}/Q_{\rm cl})^2]k_{\rm cl}}\langle F_{\rm ts}\rangle\,. \tag{18}$$

Substituting $\tilde{\omega}_{\rm drive} = 1$ yields another common form as follows [14,32]:

$$A_{\rm cl} = A_{\rm free}\sqrt{1 - 4\left(\frac{\langle F_{\rm ts}\rangle}{F_{\rm drive}|_{\tilde{\omega}=1}}\right)^2}, \tag{19}$$

where $F_{\rm drive}$ is given by

$$F_{\rm drive}|_{\tilde{\omega}=1} = \frac{A_{\rm free}k_{\rm cl}}{Q_{\rm cl}}. \tag{20}$$

It is, thus, demonstrated that the equation derived here for arbitrary $f_{\rm drive}$ includes the equations previously derived for f_0.

III. DRIVING FREQUENCY DEPENDENCE OF FORCES

In this section, we examine the frequency characteristics of the derived formula. First, in the repulsive regime, Fig. 2(a) presents the correlation between $\tilde{A}_{\rm cl}$ and the converted force at various $f_{\rm drive}$. The calculation was performed using a typical experimental condition of HS-AFM: $k_{\rm cl} = 0.1$ N/m, $f_0 = 1$ MHz, $Q_{\rm cl} = 1.5$, and $A_{\rm free} = 3$ nm$_{p\text{–}0}$. When $f_{\rm drive}$ is set to f_0, the curve is nonlinear, and the force rises steeply near $\tilde{A}_{\rm cl} = 1$. In this condition, even a slight change in the amplitude setpoint results in a significant variation in the force, making it difficult to measure accurately with a small force. In contrast, as $f_{\rm drive}$ is decreased, the force slope becomes smaller and closer to linear, making it possible to measure with a small force. Near the MaxSlope frequency, the force slope is minimized and becomes almost linear. However, as $f_{\rm drive}$ is further decreased, the slope increases once again, leading to a deterioration in force sensitivity.

Since excitation at $f_{\rm peak}$ is also commonly employed, we also calculate the force when excited at this frequency. Consequently, the force slope increases to ∼1.5 times greater than that at the MaxSlope frequency; however, it remains considerably smaller than that for excitation at f_0. This result clearly indicates that the conventional force conversion method overestimates the applied force by several times compared with the actual force when excited at either $f_{\rm peak}$ or the MaxSlope frequencies.

Furthermore, in Fig. 2(b), we also quantified the $f_{\rm drive}$ dependence of the force (normalized by these at f_0) at $\tilde{A}_{\rm cl} = 0.95$. We observed that force minima occur at a frequency lower than f_0 (see the arrows), which is referred to as the MinForce frequency ($f_{\rm MF}$). As is the case for MaxSlope, MinForce exists at both lower and upper frequencies, denoted as $f_{\rm LMF}$ and $f_{\rm UMF}$, respectively. We also found that the prominence of this minimum increases as $Q_{\rm cl}$ grows. When $Q_{\rm cl} = 1.5$, this minimum force is 1/5 of the force at f_0. This result suggests that excitation at the MinForce frequency enables imaging with minimal force.

For example, the conventional equation for f_0 estimates the interaction force at $\tilde{A}_{\rm cl} = 0.95$ to be 31 pN. This force is substantially stronger than the typical biological binding force of ∼10 pN; e.g., the binding force between myosin and F-actin is 15 pN [34]. In contrast, our improved equation estimates the interaction force at $\tilde{A}_{\rm cl} = 0.95$ to be 6.7 pN when excited at a MaxSlope frequency. This force level is below the strength of typical intermolecular bonds, demonstrating that this provides a consistent explanation for the force overestimation problem.

However, since the peak force is an order of magnitude greater than the average force (see Sec. VIII), it reaches several tens of piconewtons when converted to the peak force, still exceeding biological molecular binding forces. One possible explanation is that binding force measurements in single-molecule pulling experiments focus on localized receptor regions, whereas AFM exerts compressive forces that are distributed over a broader molecular area. Another hypothesis suggests that protein structural relaxation does not follow the period of tip interactions, as f_0 can reach up to ∼1 MHz in HS-AFM. If the tip interacts sufficiently faster than the relaxation time, which ranges from 30 to 1000 μs [49], the impact of the peak force on the molecular disruption is attenuated relative to the average force. This hypothesis is supported by single-molecule force spectroscopy studies showing that rupture force increases with loading rate [50].

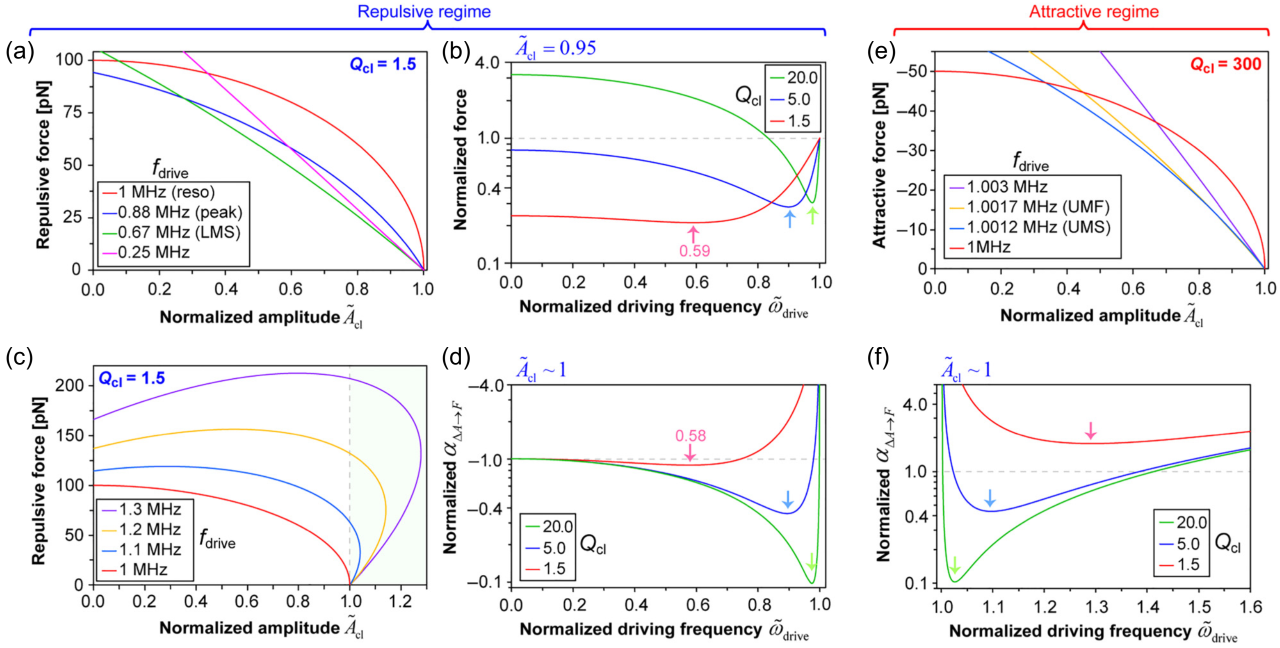

FIG. 2. (a),(c) Theoretical normalized amplitude dependence of the average repulsive force when the driving frequency is (a) below or (c) above the resonance frequency [Eq. (14)]. In the legend, "reso," "peak," and "LMS" represent resonance, peak, and lower MaxSlope frequencies, respectively. (b) Theoretical driving frequency dependence of the average repulsive force ($\tilde{A}_{cl} = 0.95$) normalized by those at the resonance frequencies. (d),(f) Driving frequency dependence of $\alpha_{\Delta A\to F}$ ($\tilde{A}_{cl} = 1$) normalized by those at 0 Hz for different Q_{cl} in (d) the repulsive and (f) attractive regimes [Eq. (23)]. The arrows in (b),(d),(f) indicate the force minima for each Q_{cl}. (e) Normalized amplitude dependence of the average attractive force [Eq. (14)]. In the legend, "UMS" and "UMF" represent the upper MaxSlope and MinForce frequencies, respectively.

For a more comprehensive understanding, in Fig. 2(c), we also conduct the calculation at frequencies exceeding f_0. The results display the characteristics of a two-valued curve, where the branch in the far region can be calculated by applying the negative sign in Eq. (14). This indicates that, as the tip approaches the surface, the amplitude undergoes an initial increase until f_0 exceeds f_{drive}, followed by a subsequent decline, as predicted from the results in Figs. 1(a) and 1(c). This causes an excessive force to be applied, even if $\tilde{A}_{cl} \sim 1$. Occasionally, this leads to the undesirable inversion of image contrast, where a lower area is observed as higher than a higher area, distorting the imaging interpretation. Note that there are also practical precautions to consider when converting amplitude values to force in experiments (Supplemental Material [51]).

Next, we derive an analytical expression for the MinForce frequencies. To obtain this formula, the force magnitude near $\tilde{A}_{cl} = 1$ in Fig. 2(a) must be examined; however, it drops to zero, making a direct comparison impossible. Instead, when excited below the resonance slope frequencies, the force increases linearly, particularly at $\tilde{A}_{cl} \sim 1$, and is approximated by

$$\langle F_{ts}\rangle \approx \left(\frac{1}{A_{free}} \lim_{\tilde{A}_{cl}\to 1} \frac{\partial\langle F_{ts}\rangle}{\partial \tilde{A}_{cl}}\right)\Delta A_{ts} \equiv \alpha_{\Delta A\to F}\Delta A_{ts}. \quad (21)$$

This equation indicates that the force magnitude is correlated with the force slope near $\tilde{A}_{cl} = 1$. Therefore, we obtain the force slope by differentiating Eq. (14) as follows:

$$\frac{\partial\langle F_{ts}\rangle}{\partial \tilde{A}_{cl}} = -\frac{k_{cl}A_{free}}{2Q_{cl}}\left[\frac{\tilde{A}_{cl}\tilde{\omega}^2_{drive}}{\sqrt{(1-\tilde{A}^2_{cl})\tilde{\omega}^2_{drive} + Q^2_{cl}(1-\tilde{\omega}^2_{drive})^2}} + Q_{cl}(1-\tilde{\omega}^2_{drive})\right]. \quad (22)$$

Then, $\alpha_{\Delta A\to F}$, which represents the conversion coefficient from ΔA_{ts} to $\langle F_{ts}\rangle$ at $\tilde{A}_{cl} = 1$, is obtained as follows:

$$\begin{aligned}\alpha_{\Delta A\to F} &\equiv \frac{1}{A_{free}} \lim_{\tilde{A}_{cl}\to 1} \frac{\partial\langle F_{ts}\rangle}{\partial \tilde{A}_{cl}} \\ &= -\frac{k_z}{2Q_{cl}}\left[\frac{\tilde{\omega}^2_{drive}}{Q_{cl}(1-\tilde{\omega}^2_{drive})} + Q_{cl}(1-\tilde{\omega}^2_{drive})\right] \\ &\quad (\tilde{\omega}_{drive} \neq 1). \end{aligned} \quad (23)$$

This equation is plotted in Fig. 2(d), which bears a close resemblance to that in Fig. 2(c). Note that Eqs. (22) and (23) are valid only for $\tilde{\omega}_{drive} < 1$ and $\tilde{\omega}_{drive} > 1$ in the repulsive and attractive regimes, respectively. By solving $\partial \alpha_{\Delta A \to F} / \partial \tilde{\omega}_{\mathrm{drive}} = 0$, the MinForce frequencies are obtained as follows [see the arrows in Fig. 2(d)]:

$$\tilde{\omega}_{\mathrm{LMF}} = \frac{f_{\mathrm{LMF}}}{f_0} = \sqrt{1 - \frac{1}{Q_{\mathrm{cl}}}} \quad (Q_{\mathrm{cl}} \geq 1), \tag{24}$$

$$\tilde{\omega}_{\mathrm{UMF}} = \frac{f_{\mathrm{UMF}}}{f_0} = \sqrt{1 + \frac{1}{Q_{\mathrm{cl}}}}. \tag{25}$$

Importantly, this analysis revealed that the MinForce frequencies can be expressed by straightforward analytical equations.

Previous studies have reported an equation describing the frequency dependence of peak force based on the Hertzian model approximation [24,38]. While this equation enables the calculation of a peak force without time-consuming experiments, its applicability is limited to simple geometries where the Hertzian theory holds. Additionally, various parameters such as Young's modulus and the shape of both the tip and the sample must be assumed. Using the same frequency analysis, we found that the MinForce frequencies of the peak force are also given by Eqs. (24) and (25) (Sec. VIII). Thus, excitation at the MinForce frequency maximizes force detection sensitivity for both the average and peak forces.

A previous study empirically derived a linear approximation for force conversion at off-resonance frequencies based on simulation results, i.e., [36]

$$\langle F_{\mathrm{ts}} \rangle_{\text{off-reso}} = -\frac{k_{\mathrm{cl}}}{2Q_{\mathrm{eff}}} \Delta A_{\mathrm{ts}}, \tag{26}$$

where Q_{eff} denotes the effective Q_{cl}, which can be derived from Eq. (9) as follows:

$$Q_{\mathrm{eff}} = \frac{1}{\sqrt{\left(1 - \tilde{\omega}_{\mathrm{drive}}^2\right)^2 + \left(\tilde{\omega}_{\mathrm{drive}}/Q_{\mathrm{cl}}\right)^2}}. \tag{27}$$

When $\tilde{\omega}_{\mathrm{drive}} = 1$, Q_{eff} equals Q_{cl} whereas, when $\tilde{\omega}_{\mathrm{drive}} = 0$, Q_{eff} decreases to 1.

In the following steps, we demonstrate that Eq. (26) can be derived from Eq. (23). By solving Eq. (27) for $\tilde{\omega}_{\mathrm{drive}}$, the following expression is obtained:

$$\tilde{\omega}_{\mathrm{drive}} = \sqrt{1 - \frac{1}{2Q_{\mathrm{cl}}^2} - \sqrt{\frac{1}{4Q_{\mathrm{cl}}^4} - \frac{1}{Q_{\mathrm{cl}}^2} + \frac{1}{Q_{\mathrm{eff}}^2}}}. \tag{28}$$

When Q_{cl} is sufficiently large (typically $Q_{\mathrm{cl}} > 10$), it can be approximated as follows:

$$\lim_{Q_{\mathrm{cl}} \to \infty} \tilde{\omega}_{\mathrm{drive}} \approx \sqrt{1 - \frac{1}{Q_{\mathrm{eff}}}}. \tag{29}$$

Substituting this into Eq. (23) yields:

$$\alpha_{\Delta A \to F}|_{\text{off-reso}} = -\frac{k_{\mathrm{cl}}}{2Q_{\mathrm{cl}}} \left(\frac{Q_{\mathrm{eff}}}{Q_{\mathrm{cl}}} + \frac{Q_{\mathrm{cl}}}{Q_{\mathrm{eff}}} - \frac{1}{Q_{\mathrm{cl}}} \right). \tag{30}$$

Again, by taking the limit as $Q_{\mathrm{cl}} \to \infty$, this equation can be simplified as follows:

$$\lim_{Q_{\mathrm{cl}} \to \infty} \alpha_{\Delta A \to F}|_{\text{off-reso}} = -\frac{k_{\mathrm{cl}}}{2Q_{\mathrm{eff}}}. \tag{31}$$

Substituting this into Eq. (21) yields Eq. (26), which provides a good approximation when f_{drive} is smaller than the MinForce frequency, indicating that Eq. (23) encompasses Eq. (26).

Next, the attractive regime is also analyzed. Since it is only utilized under ambient environments, typical values for ambient AM-AFM of $Q_{\mathrm{cl}} = 300$ and $k_{\mathrm{cl}} = 3$ N/m are used. In Fig. 2(e), we obtained results showing nearly the same tendency as the repulsive force presented in Fig. 2(a). When excited at f_0, the force increases steeply at $\tilde{A}_{\mathrm{cl}} = 1$ but, as f_{drive} increases, the force slope becomes smaller and approaches linearity. When f_{drive} exceeds the upper MinForce frequency, the force slope increases again. In Fig. 2(f), we also examine the $\tilde{\omega}_{\mathrm{drive}}$ dependence of the force slope and obtained results similar to those for the repulsive regime in Fig. 2(d), except that the curves are inverted along the x-axis. Another notable difference is that, while the values converge to a constant at low frequencies in the repulsive regime, they diverge at high frequencies in the attractive regime.

IV. SIMPLIFIED FORCE CONVERSION METHOD

Substituting Eqs. (24) and (25) into Eq. (14) gives simplified conversion equations from amplitude values to the force at MinForce, i.e.,

$$\langle F_{\mathrm{ts}} \rangle_{\mathrm{LMF}} = \frac{k_{\mathrm{cl}} A_{\mathrm{free}}}{2Q_{\mathrm{cl}}} \left[-\tilde{A}_{\mathrm{cl}} + \sqrt{1 + \left(1 - \frac{1}{Q_{\mathrm{cl}}}\right)\left(1 - \tilde{A}_{\mathrm{cl}}^2\right)} \right] \quad (Q_{\mathrm{cl}} \geq 1), \tag{32}$$

$$\langle F_{\mathrm{ts}} \rangle_{\mathrm{UMF}} = -\frac{k_{\mathrm{cl}} A_{\mathrm{free}}}{2Q_{\mathrm{cl}}} \left[-\tilde{A}_{\mathrm{cl}} + \sqrt{1 + \left(1 + \frac{1}{Q_{\mathrm{cl}}}\right)\left(1 - \tilde{A}_{\mathrm{cl}}^2\right)} \right]. \tag{33}$$

By calculating the derivative according to Eq. (23), $\alpha_{\Delta A \to F}$ are obtained as follows:

$$\alpha_{\Delta A \to F}(\tilde{\omega}_{\mathrm{LMF}}) = -\frac{k_{\mathrm{cl}}}{2Q_{\mathrm{cl}}} \left(2 - \frac{1}{Q_{\mathrm{cl}}}\right) \quad \text{if } \langle F_{\mathrm{ts}} \rangle > 0, \tag{34}$$

$$\alpha_{\Delta A \to F}(\tilde{\omega}_{\mathrm{UMF}}) = \frac{k_{\mathrm{cl}}}{2Q_{\mathrm{cl}}} \left(2 + \frac{1}{Q_{\mathrm{cl}}}\right) \quad \text{if } \langle F_{\mathrm{ts}} \rangle < 0. \tag{35}$$

These equations represent the force conversion at the frequency where the force detection sensitivity is maximized.

To convert amplitudes into forces, the nonlinear equations presented in Eqs. (14), (32), or (33) are generally required. However, a linear approximation of Eq. (21) can be conveniently applied when exciting at a resonance slope frequency, at which $\alpha_{\Delta A \to F}$ can be readily calculated using Eqs. (34) or (35). For a typical HS-AFM parameter of $Q_{\mathrm{cl}} = 1.5$, the force can be calculated as follows:

$$\begin{aligned} \langle F_{\mathrm{ts}} \rangle_{\mathrm{LMF}} &\approx -0.444 k_{\mathrm{cl}} \Delta A_{\mathrm{ts}} \\ &= 0.444 k_{\mathrm{cl}} A_{\mathrm{free}} (1 - \tilde{A}_{\mathrm{cl}}). \end{aligned} \tag{36}$$

By setting other typical values, $k_{\mathrm{cl}} = 0.1$ N/m and $A_{\mathrm{free}} = 3$ $\mathrm{nm}_{\mathrm{p-0}}$, a more practical expression can be obtained as follows:

$$\langle F_{\mathrm{ts}} \rangle_{\mathrm{LMF}} \approx 133 \times 10^{-12} (1 - \tilde{A}_{\mathrm{cl}}). \tag{37}$$

Using this equation, for example, we can easily estimate F_{ts} to be 6.7 and 13.3 pN for $\tilde{A}_{\mathrm{cl}} = 0.95$ and 0.9, respectively. The force of 6.7 pN is consistent with the value of 6.6 pN predicted by the nonlinear equation in Eq. (32).

V. COMPARISON BETWEEN MINFORCE AND MAXSLOPE FREQUENCIES

Since excitation is conventionally performed at the MaxSlope frequency [1], we next need to identify the frequency offering the greatest advantage. To predict the MaxSlope frequency, we must solve the second-order differential equation of A_{cl} [Eq. (9)], i.e.,

$$\begin{aligned} \frac{\partial^2 A_{\mathrm{cl}}(\tilde{\omega}_{\mathrm{drive}})}{\partial \tilde{\omega}_{\mathrm{drive}}^2} &= A_0 \left\{ \frac{3\tilde{\omega}_{\mathrm{drive}}^2 [2(1 - \tilde{\omega}_{\mathrm{drive}}^2) - 1/Q_{\mathrm{cl}}^2]^2}{[(1 - \tilde{\omega}_{\mathrm{drive}}^2)^2 + (\tilde{\omega}_{\mathrm{drive}}/Q_{\mathrm{cl}})^2]^{5/2}} \right. \\ &\quad \left. + \frac{2(1 - \tilde{\omega}_{\mathrm{drive}}^2) - 1/Q_{\mathrm{cl}}^2 - 4\tilde{\omega}_{\mathrm{drive}}^2}{[(1 - \tilde{\omega}_{\mathrm{drive}}^2)^2 + (\tilde{\omega}_{\mathrm{drive}}/Q_{\mathrm{cl}})^2]^{3/2}} \right\} \\ &= 0. \end{aligned} \tag{38}$$

Unfortunately, this equation is difficult to solve using elementary functions. However, when Q_{cl} is sufficiently large ($Q_{\mathrm{cl}} > 10$), A_{cl} in Eq. (9) can be approximated by a Lorentzian function as follows:

$$\lim_{Q_{\mathrm{cl}} \to \infty} A_{\mathrm{cl}}(\tilde{\omega}_{\mathrm{drive}}) = \frac{A_0}{\sqrt{4(1 - \tilde{\omega}_{\mathrm{drive}})^2 + 1/Q_{\mathrm{cl}}^2}}, \tag{39}$$

which is given by a Taylor series approximation. With this equation, the differential equation above can be analytically solved as follows [1]:

$$\lim_{Q_{\mathrm{cl}} \to \infty} \tilde{\omega}_{\mathrm{LMS}} = \lim_{Q_{\mathrm{cl}} \to \infty} \frac{f_{\mathrm{LMS}}}{f_0} \approx 1 - \frac{1}{\sqrt{8} Q_{\mathrm{cl}}}, \tag{40}$$

$$\lim_{Q_{\mathrm{cl}} \to \infty} \tilde{\omega}_{\mathrm{UMS}} = \lim_{Q_{\mathrm{cl}} \to \infty} \frac{f_{\mathrm{UMS}}}{f_0} \approx 1 + \frac{1}{\sqrt{8} Q_{\mathrm{cl}}}. \tag{41}$$

This approximation cannot be applied to liquid AM-AFM, where Q_{cl} is substantially reduced (1.5 for typical HS-AFM experiments). Therefore, by expanding these approximate solutions with the numerically calculated solution of Eq. (38), we obtained a Laurent polynomial approximation for the lower MaxSlope ($\tilde{\omega}_{\mathrm{LMS}}$), i.e.,

$$\begin{aligned} \tilde{\omega}_{\mathrm{LMS}} \approx 1 - \frac{1}{Q_{\mathrm{cl}}} \Bigg[& \frac{1}{\sqrt{8}} + \frac{0.2148}{Q_{1/2}} - \left(\frac{0.3074}{Q_{1/2}} \right)^2 \\ & + \left(\frac{0.2739}{Q_{1/2}} \right)^3 - \left(\frac{0.2016}{Q_{1/2}} \right)^4 + \left(\frac{0.1715}{Q_{1/2}} \right)^{12} \Bigg], \end{aligned} \tag{42}$$

where $Q_{1/2} = Q_{\mathrm{cl}} - 1/2 \quad \left(Q_{\mathrm{cl}} \geq 1/\sqrt{2} \right)$, which is valid for arbitrary Q_{cl}. When $Q_{\mathrm{cl}} = 1/\sqrt{2}$, $\tilde{\omega}_{\mathrm{LMS}}$ drops to zero. In contrast, the Q_{cl} dependency of the upper MaxSlope ($\tilde{\omega}_{\mathrm{UMS}}$) forms a biphasic curve. Therefore, by switching two equations between high and low Q_{cl}, it can be analytically expressed over the entire Q_{cl} range (Supplemental Material [51]). The equation for high Q_{cl}, which is significant in experiments, is given as follows:

$$\begin{aligned} \tilde{\omega}_{\mathrm{UMS}} \approx 1 + \frac{1}{Q_{\mathrm{cl}}} \Bigg[& \frac{1}{\sqrt{8}} - \frac{0.2194}{Q_{1/4}} + \left(\frac{0.2294}{Q_{1/4}} \right)^2 \\ & - \left(\frac{0.2547}{Q_{1/4}} \right)^3 + \left(\frac{0.2131}{Q_{1/4}} \right)^4 \Bigg], \end{aligned} \tag{43}$$

where $Q_{1/4} = Q_{\mathrm{cl}} - 1/4$, which is valid for arbitrary Q_{cl} greater than 0.5.

Next, we compare the Q_{cl} dependence of the MinForce and MaxSlope frequencies in the repulsive regime. In Fig. 3(a), as Q_{cl} decreases, the lower MinForce frequency steeply falls to 0 even at $Q_{\mathrm{cl}} = 1$, while the MaxSlope frequency remains above 0.4 at $Q_{\mathrm{cl}} > 1$. Moreover, the forces normalized by those at f_0 are compared in Fig. 3(b), exhibiting that there is almost no significant difference across the entire Q_{cl} value. It can be seen that the force at f_{peak} is several times larger than them. For ease of understanding, the values for a typical HS-AFM parameter ($Q_{\mathrm{cl}} = 1.5$) are also shown in Figs. 3(a) and 3(b). A notable discrepancy is observed in the frequencies, with a difference of 0.09 (=0.67 − 0.58) between the MaxSlope and MinForce. In contrast, the difference in forces is relatively minor, at 0.01 (=0.22 − 0.21). This illustrates a significant contrast between the two variables.

We also performed the same analysis in the attractive regime. In Fig. 3(c), the result clearly indicates that the

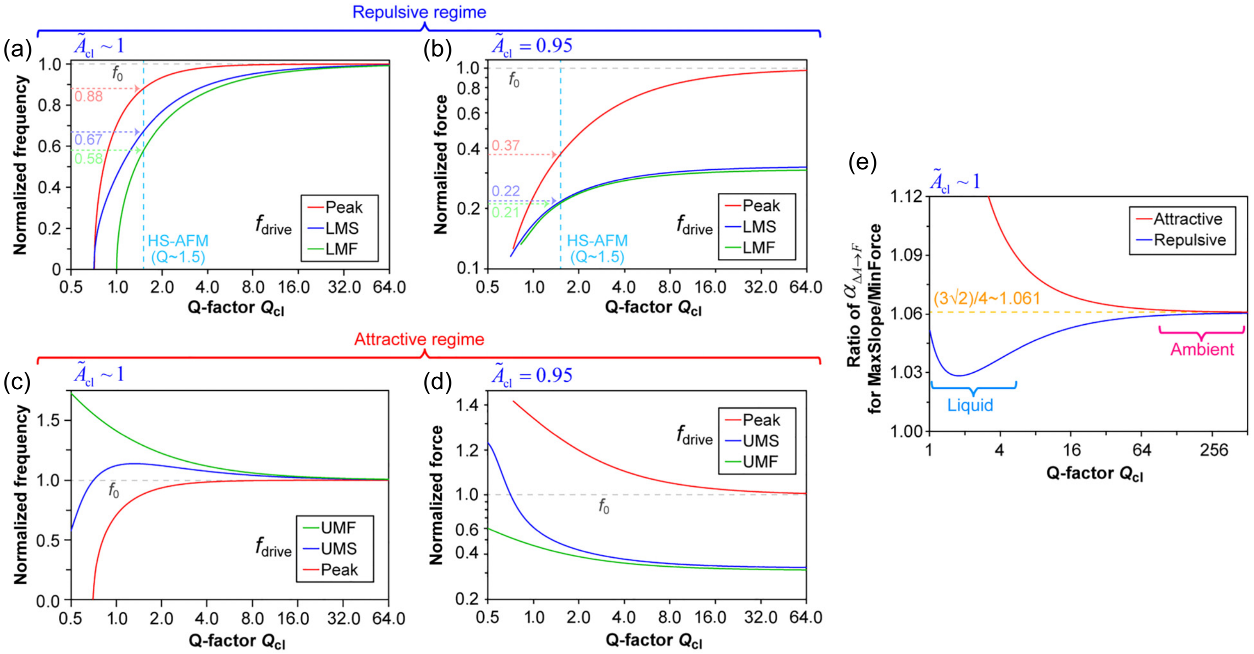

FIG. 3. (a),(c) Theoretical $Q_{\rm cl}$ dependence of characteristic frequencies normalized by the resonance frequencies (f_0) in (a) the repulsive and (c) attractive regimes. (b),(d) Theoretical $Q_{\rm cl}$ dependence of the average force ($\tilde{A}_{\rm cl} = 0.95$) that is normalized by those at the resonance in (b) the repulsive and (d) attractive regimes. In the legend, "LMS" and "LMF" represent the lower MaxSlope and MinForce frequencies, respectively, and "UMS" and "UMF" represent the upper MaxSlope and MinForce frequencies, respectively. The dashed horizontal lines indicate the results at f_0. (e) $Q_{\rm cl}$ dependence of the ratio of $\alpha_{\Delta A \to F}$ between the MaxSlope and MinForce frequencies, with the lower and upper frequencies used for the repulsive and attractive regimes, respectively.

upper MinForce frequency is higher than the upper MaxSlope frequency at all $Q_{\rm cl}$. As $Q_{\rm cl}$ decreases, the upper MinForce frequency increases monotonically while the upper MaxSlope frequency increases once and then decreases. In Fig. 3(d), when analyzing the forces normalized by those at f_0, contrary to the repulsive regime, there is a distinct difference between the two forces at $Q_{\rm cl} < 4$. However, as $Q_{\rm cl}$ increases, both the forces asymptotically approach the same value, similar to the repulsive regime.

To compare the two forces more quantitatively, the $Q_{\rm cl}$ dependence of the ratio of $\alpha_{\Delta A \to F}$ at the MaxSlope and MinForce frequencies is examined in Fig. 3(e). In the repulsive regime, the ratio ranges from 1.03 to 1.06 for all $Q_{\rm cl}$ values, showing no significant $Q_{\rm cl}$ dependence. In the attractive regime, however, the ratio decreases steeply with decreasing $Q_{\rm cl}$. Both the ratios asymptotically approach 1.061, which can be obtained analytically in the following steps. In the large $Q_{\rm cl}$ limit, $\alpha_{\Delta A \to F}$ for MinForce can be obtained from Eqs. (34) and (35) as follows:

$$\lim_{Q_{\rm cl}\to\infty} \alpha_{\Delta A \to F}(\tilde{\omega}_{\rm LMF}) = -\frac{k_{\rm cl}}{Q_{\rm cl}} \quad \text{if } \langle F_{\rm ts} \rangle > 0, \tag{44}$$

$$\lim_{Q_{\rm cl}\to\infty} \alpha_{\Delta A \to F}(\tilde{\omega}_{\rm UMF}) = \frac{k_{\rm cl}}{Q_{\rm cl}} \quad \text{if } \langle F_{\rm ts} \rangle < 0. \tag{45}$$

For MaxSlope, these can be found by substituting Eqs. (40) and (41) into Eq. (23), yielding

$$\lim_{Q_{\rm cl}\to\infty} \alpha_{\Delta A \to F}(\tilde{\omega}_{\rm LMS}) = -\frac{k_{\rm cl}}{Q_{\rm cl}}\frac{3\sqrt{2}}{4} \quad \text{if } \langle F_{\rm ts} \rangle > 0, \tag{46}$$

$$\lim_{Q_{\rm cl}\to\infty} \alpha_{\Delta A \to F}(\tilde{\omega}_{\rm UMS}) = \frac{k_{\rm cl}}{Q_{\rm cl}}\frac{3\sqrt{2}}{4} \quad \text{if } \langle F_{\rm ts} \rangle < 0. \tag{47}$$

Consequently, the value of 1.061 can be obtained as follows:

$$\lim_{Q_{\rm cl}\to\infty} \frac{\alpha_{\Delta A \to F}(\tilde{\omega}_{\rm LMS})}{\alpha_{\Delta A \to F}(\tilde{\omega}_{\rm LMF})} = \lim_{Q_{\rm cl}\to\infty} \frac{\alpha_{\Delta A \to F}(\tilde{\omega}_{\rm UMS})}{\alpha_{\Delta A \to F}(\tilde{\omega}_{\rm UMF})} = \frac{3\sqrt{2}}{4} \approx 1.061, \tag{48}$$

Although the force sensitivity of MinForce is slightly higher than that of MaxSlope, our results indicate that the difference is only ∼3% in liquid and ∼6% in air, which may fall within the error margin. The results indicate that the approximate equation for MinForce can be employed either when excited at the MaxSlope or MinForce frequency.

VI. NUMERICAL SIMULATION-BASED VALIDATION OF THEORY

To validate the applicability of the derived theory, we conducted numerical simulations based on the Hertzian theory for contact between a sphere and an infinite plane, i.e., [29,56–58]

$$F_{\mathrm{Hertz}}(\delta) = \frac{4E^*}{3}\sqrt{R_{\mathrm{tip}}}(-\delta)^{3/2}, \tag{49}$$

where R_{tip} and δ are the radius of curvature of the tip and indentation depth, respectively, and E^* is the reduced Young's modulus, expressed as

$$E^* = \left(\frac{1-\nu_s^2}{E_s} + \frac{1-\nu_{\mathrm{tip}}^2}{E_{\mathrm{tip}}}\right)^{-1}, \tag{50}$$

where ν and E represent the Poisson's ratio and Young's modulus, respectively, where the subscripts s and tip denote the sample and tip, respectively. When the tip is sufficiently rigid compared with the sample, E^* can be approximated as follows:

$$E^* \approx \frac{E_s}{1-\nu_s^2}. \tag{51}$$

By assuming a typical value of 0.33 for ν_s of globular proteins [59,60], E^* is comparable with E_s as follows:

$$E^* \approx 1.122E_s. \tag{52}$$

We first examine the distance dependence of Eq. (49), which exhibits that F_{ts} increases as the distance decreases, with the force gradient scaling proportionally to E^* [Fig. 4(a)]. Subsequently, we simulated the equation of motion [Eq. (1)] coupling with Eq. (49) using the velocity Verlet algorithm and typical HS-AFM parameters: $k_{\mathrm{cl}} = 0.1$ N/m, $Q_{\mathrm{cl}} = 1.5$, $R_{\mathrm{tip}} = 5$ nm, and $A_{\mathrm{free}} = 3$ $\mathrm{nm}_{\mathrm{p-0}}$. The average forces were calculated from the time-averaged deflection. In Figs. 4(b) and 4(c), when $\tilde{A}_{\mathrm{cl}} > 0.5$, good agreement between simulation and analytical solutions is obtained at both the MinForce and resonance frequencies for $E^* \geq 100$ MPa. In contrast, when $E^* \leq 10$ MPa, good agreement is limited to values of $\tilde{A}_{\mathrm{cl}} > 0.8$. In nondestructive biomolecular imaging, $\tilde{A}_{\mathrm{cl}}$ is typically set to 0.9 or more, indicating that this force conversion method can be adapted to a wide range of systems, even though the equation does not incorporate Young's modulus as a variable.

Furthermore, proteins and nucleic acids, which are the most amenable to HS-AFM observation, generally have E_s on the order of gigapascals. Although lipid membranes and liposomes in a fluid phase have E_s of several megapascals, the apparent E_s in AFM experiments is an order of magnitude higher than the actual value due to the bottom effect [57,58]. Therefore, it is rare for the observed target to have E_s of less than 10 MPa.

For comparison, similar simulations were conducted for the peak force (Supplemental Material [51]). Unlike the average force, it was observed that the peak force shows a significant dependence on E^*, even when $\tilde{A}_{\mathrm{cl}}$ is close to 1. This indicates that, while estimating the peak force experimentally requires assuming E^* and R_{tip}, the estimation of the average force can achieve sufficient accuracy using an approximation that does not account for the E^* dependence.

Note that in Figs. 4(b) and 4(c), with $E^* = 1$ GPa, some steplike jumps are observed that are not reproduced in the analytical solution. A frequency spectrum analysis revealed that this discontinuous change in amplitude occurs when f_0 is shifted by the interaction and coincides with a harmonic frequency of the excitation frequency.

For the simulation in the attractive regime, we used the Derjaguin, Muller, Toporov, and Maugis (DMT-M) theory [29], where the force F_{DMT} is given by

$$F_{\mathrm{DMT}}(z) = \begin{cases} F_{\mathrm{vdW}}(z) & \text{for } z \geq z_0, \\ F_{\mathrm{Hertz}}(z_0 - z) + F_{\mathrm{vdW}}(z_0) & \text{otherwise,} \end{cases} \tag{53}$$

where the van der Waals force (F_{vdW}) is expressed by

$$F_{\mathrm{vdW}}(z) = -\frac{A_{\mathrm{H}}^* R_{\mathrm{tip}}}{6z^2}. \tag{54}$$

The effective Hamaker constant A_{H}^* is calculated from those of sample $A_{\mathrm{H}}^{\mathrm{s}}$ and tip $A_{\mathrm{H}}^{\mathrm{tip}}$ as follows:

$$A_{\mathrm{H}}^* = \sqrt{A_{\mathrm{H}}^{\mathrm{s}} A_{\mathrm{H}}^{\mathrm{tip}}}. \tag{55}$$

Typical values of A_{H} range between 20 to 500 zJ [61], with hydrocarbons having 20–100 zJ, oxides having 60–200 zJ, and metals having 200–500 zJ.

The calculations were conducted with typical ambient AM-AFM parameters: $R_{\mathrm{tip}} = 5$ nm, $A_{\mathrm{free}} = 10$ $\mathrm{nm}_{\mathrm{p-0}}$, $E^* = 10$ GPa, and $z_0 = 0.5$ nm. In Fig. 4(d), the calculated force curve showed a gradual increase in the attractive force as the tip approaches the surface, with the magnitude of the attractive force increasing in proportion to A_{H}^*. Subsequently, as the tip enters the Hertzian contact regime, the force exhibits a notable positive increase.

Subsequently, we performed simulations for the attractive regime using Eq. (53), following the repulsive regime. In Fig. 4(e), the simulation and the analytical results for MinForce were in better agreement for all A_{H}. For the result of f_0 [Fig. 4(f)], although a similar nonlinear shape is observed, the analytical solution slightly overestimates the force, suggesting that the analytical calculation is valid only for the MaxSlope and MinForce frequencies in the

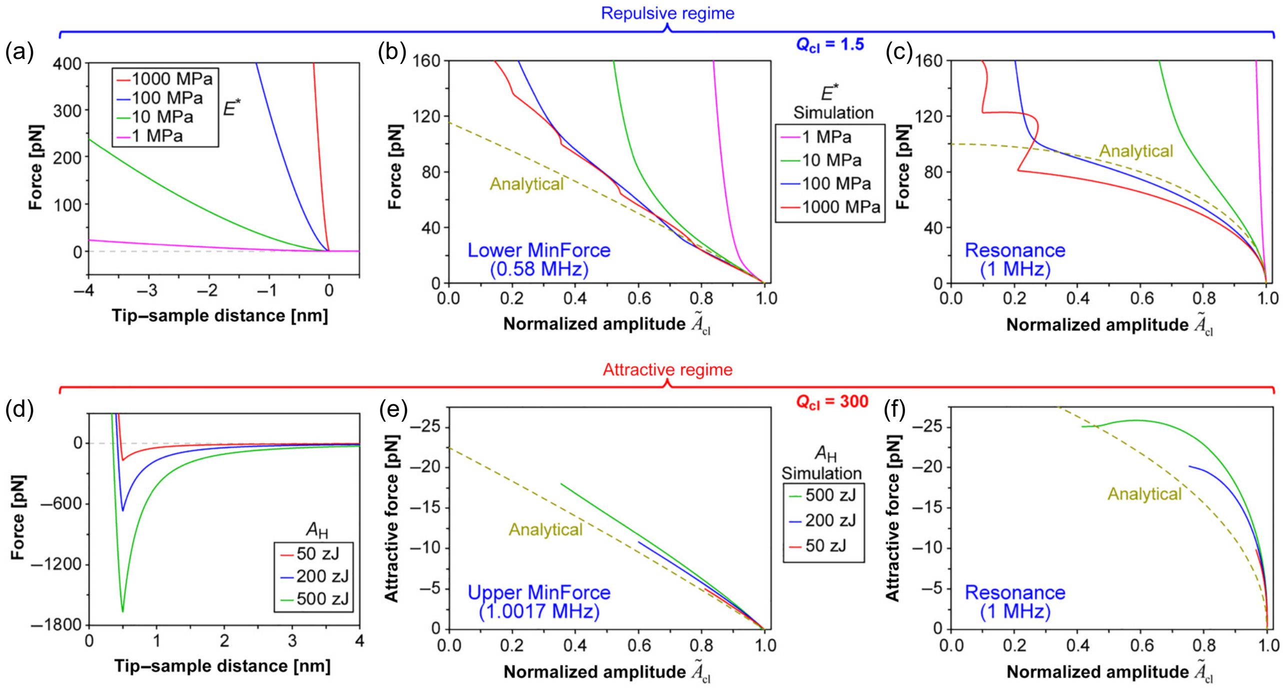

FIG. 4. (a),(d) Force-distance curves used in the simulations in (a) the repulsive and (d) attractive regimes, performed based on the Hertzian and DMT models, respectively. (b),(c),(e),(f) Numerical simulation and analytical results of force as a function of normalized amplitude in (b),(c) the repulsive and (e),(f) attractive regimes when the driving frequency is at (b),(e) the MinForce and (c),(f) resonance frequencies. The analytical calculations are represented by Eq. (14).

attractive regime. Considering the above results, we can conclude that the approximate value of the force can be obtained using this analytical equation for both the repulsive and attractive regimes, particularly when excited at the MaxSlope and MinForce frequencies.

VII. EXPERIMENTAL VALIDATION OF THE THEORY

To validate the applicability of the force conversion to practical experiments, where nonideal effects can occur, we performed force curve measurements using a home-built HS-AFM setup [21], whose operational principles are identical to those of conventional AM-AFM. We used a small cantilever (BLAC10DS-A2, Olympus) with f_0 of 682 kHz, Q_{cl} of 1.8, and k_{cl} of 0.13 N/m, which were determined from a thermal spectrum [62]. To compare the static and dynamic forces quantitatively, it is important to consider the dynamic-to-static correction factors χ and ξ for the optical lever sensitivity and the spring constant, respectively [63]. However, we did not apply any corrections for k_{cl}, as these two coefficients are assumed to cancel each other out in our setup for the following reason. The correction for the spring constant is expressed as $\xi\ \chi^2$, where the factor χ takes a fixed value of ~1.03, while ξ depends on the position of the laser spot on the cantilever. Since we used a small cantilever with a length of ~10 μm, which is the same as the laser spot size, the laser was irradiated at the center, resulting in ξ being ~0.97 [64]. By taking these values, $\xi\ \chi^2$ is calculated to be 1.03, which appears to fall within the experimental error.

The cantilever was dynamically excited using the piezoacoustic method with an A_{free} of 2.8 ± 0.1 nm at various f_{drive} from 217 to 960 kHz, which correspond to $\tilde{\omega}_{\text{drive}}$ ranging from 0.32 to 1.41. For the deflection signal acquisition, a fourth-order low-pass filter was used to prevent the oscillation signal from entering the AD converter. Mica was used as the substrate due to its relatively high E_s and its common use as a supporting substrate for biomolecules. The tip was brought close to the sample surface at a constant velocity of 1.5 μm/s and returned to the farthest position when the deflection reached a threshold value of 2.7 nm, corresponding to an average force of 350 pN. To suppress instrumental noise, the averages of 300 successively measured curves were calculated.

Using the experimental conditions described above, the correlation between the force and amplitude is examined in Fig. 5(a), which demonstrated that, as the amplitude decreased, the force tended to increase, as theoretically predicted. Below f_{peak}, the force slope at $\tilde{A}_{cl} \sim 1$ became linear and varied as a function of f_{drive}. In contrast, above f_{peak}, the force slope increased markedly, resulting in a nonlinear curve. Furthermore, as $\tilde{\omega}_{\text{drive}}$ reached 1.2, $\tilde{A}_{cl}$ became

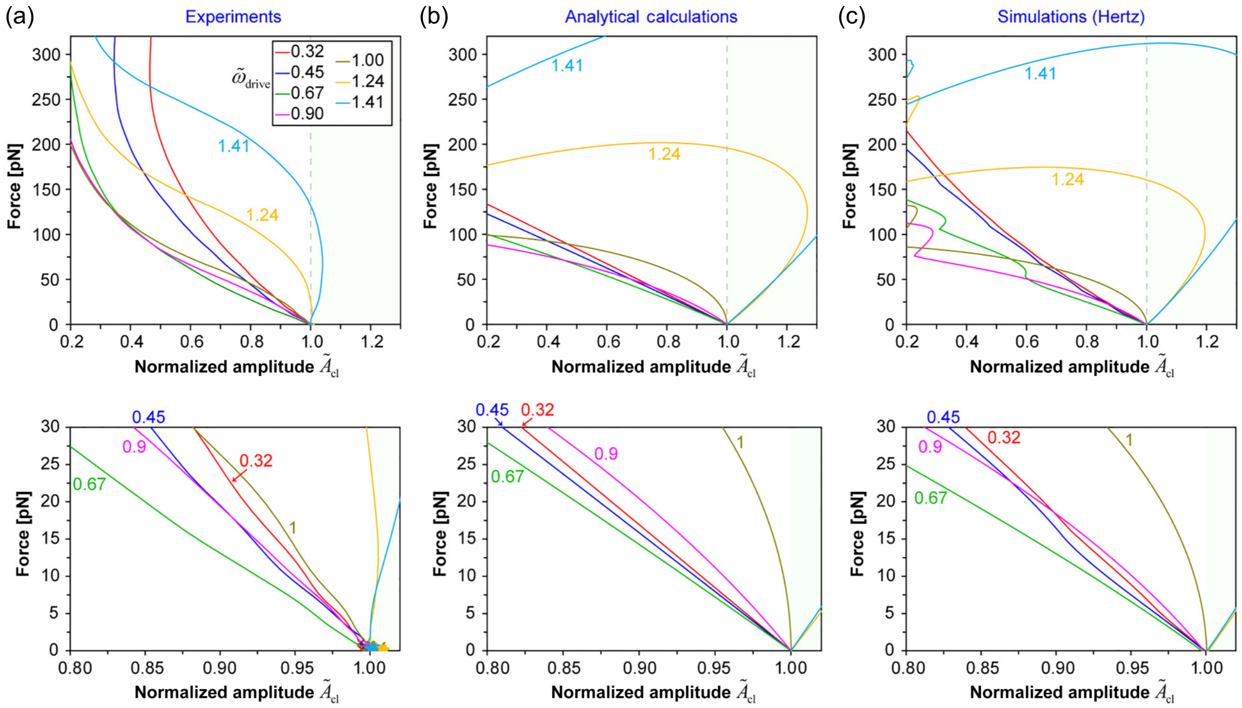

FIG. 5. (a)–(c) Comparison of (a) experiment, (b) analytical calculation, and (c) simulation of the amplitude dependence of the mean force using various driving frequencies. The magnified graphs near $\tilde{A}_{\rm cl} = 0.9$ are displayed in the lower section. The correspondence between the driving and characteristic frequencies is illustrated in Fig. 6.

greater than 1, indicating a two-valued curve, as predicted by the theory. Note that the original force curve data have been analyzed elsewhere [65].

To validate the quantitative agreement between the experiments and theory, we performed analytical calculations and simulations under the same conditions as the experiments. Here, E^* was set at 800 MPa, determined experimentally using static-mode AFM with the same threshold as that used in the dynamic-mode AFM experiments (Supplemental Material [51]). This value is smaller than the bulk mica value of 60 GPa [66], possibly because the apparent E_s depends on the loading force [67], which was small in this experiment.

The analytical results shown in Fig. 5(b) exhibit a high degree of similarity to those of the experiments conducted below $f_{\rm peak}$. However, above $f_{\rm peak}$, they exhibit a more pronounced two-valued characteristic than the experiments. The simulation results in Fig. 5(c) are almost the same as the analytical results, except that the amplitude and force above $f_{\rm peak}$ are slightly attenuated (Supplemental Material [51] for the complete graph). To elucidate this discrepancy, the $\tilde{\omega}_{\rm drive}$ dependence of the force at $\tilde{A}_{\rm cl} = 0.9$ is plotted in Fig. 6. This reveals that all results, including the experimental data, exhibit a concave-shaped curve near the lower MaxSlope and MinForce frequencies as the vertex. The discrepancy between the experiment and the analytical calculation at the force minimum is only ∼10%, which falls within the measurement error of AFM. Consequently, it is determined that the analytical calculation provides a sufficient approximation.

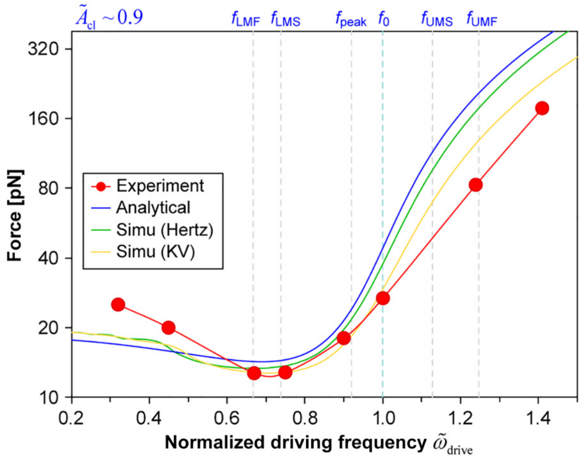

FIG. 6. Comparison of the experimental data, analytical calculations, and simulations using the Hertzian and Kelvin-Voigt (KV) models for the dependence of average force on driving frequency at $\tilde{A}_{\rm cl} = 0.9$. The standard error of the experimental data, ranging from 0.19 to 0.42 pN, is comparable with the line thickness; thus, error bars are omitted.

However, compared with theory, the experiment shows that the force at low frequencies is larger, while the force at high frequencies is smaller. The former discrepancy appears to be attributable to cantilever base oscillation, while the latter seems to result from dissipative effects not accounted for in the theory, as they manifest only when the tip makes hard contact with the sample. To substantiate this hypothesis, we also conducted simulations incorporating dissipative effects using the Kelvin-Voigt model (Supplemental Material [51]). The simulation results with the viscosity of 30 Pa s are also displayed in Fig. 6. This shows that the force above f_0 is effectively suppressed and is in close agreement with the experimental results. In summary, the analytical solution does not hold above f_{peak}; however, it provides a satisfactory approximation when excited at the resonance slope.

VIII. CONVERSION FROM AVERAGE TO PEAK FORCE

In previous studies, peak force has been considered to contribute more significantly than average force ($\langle F_{\text{ts}}\rangle$) to the disruption of biomolecules [22,24]. As discussed in Section 3, the contribution of average force may become more dominant as f_0 increases. However, since peak force remains crucial in many experimental systems, this section outlines a method to convert average force to peak force. Previous studies have reported an equation for the repulsive peak force ($F_{\text{peak}}^{\text{Hertz}}$) based on the Hertzian model approximation [24,38]. Rearranging this equation, we obtain a form similar to Eq. (14), which is written as

$$F_{\text{peak}}^{\text{Hertz}} = 2^{1/8}\left(\frac{\pi^3}{3}k_{\text{cl}}^3 E^* \sqrt{R_{\text{tip}}}\right)^{1/4} A_{\text{free}}^{9/8}\tilde{A}_{\text{cl}}^{3/8}\left\{-(1-\tilde{\omega}_{\text{drive}}^2)\tilde{A}_{\text{cl}} + \sqrt{(1-\tilde{\omega}_{\text{drive}}^2)^2 + (\tilde{\omega}_{\text{drive}}/Q_{\text{cl}})^2(1-\tilde{A}_{\text{cl}}^2)}\right\}^{3/4}. \tag{56}$$

Following the calculation of the average force, we attempted to differentiate with respect to $\tilde{A}_{\text{cl}}$ and substitute $\tilde{A}_{\text{cl}} = 1$; however, unlike the average force, this causes $\partial F_{\text{peak}}^{\text{Hertz}}/\partial \tilde{A}_{\text{cl}}$ to diverge to infinity. Nevertheless, in Eq. (56), the expression inside the brackets for the 3/4 power shares the same shape as Eq. (14), suggesting that the following approximation is valid:

$$\lim_{\tilde{A}_{\text{cl}}\to 1} F_{\text{peak}}^{\text{Hertz}} \propto \left(\lim_{\tilde{A}_{\text{cl}}\to 1} \langle F_{\text{ts}}\rangle\right)^{3/4} \approx (\alpha_{\Delta A\to F}\Delta A_{\text{ts}})^{3/4}. \tag{57}$$

This equation indicates that both forces exhibit the same frequency dependence and the MinForce frequencies derived in Eqs. (24) and (25) are valid for both.

However, while average force can be directly determined solely from experimental parameters, peak force depends on multiple factors that are difficult to measure directly, namely E^* and R_{tip}, making accurate estimation less meaningful. Moreover, even rough estimation from amplitude values is not straightforward due to the fractional power function of peak force. Therefore, we propose a convenient method to convert average force to peak force, as described below.

The conversion coefficient, $\alpha_{\text{Avg}\to\text{Peak}}$, from average to peak force is defined as follows:

$$\alpha_{\text{Avg}\to\text{Peak}} = \frac{F_{\text{peak}}}{\langle F_{\text{ts}}\rangle}. \tag{58}$$

Using analytical solutions from Eqs. (14) and (56) with typical HS-AFM parameters (i.e., $E^* = 1000$ MPa, $R_{\text{tip}} = 5$ nm, $k_{\text{cl}} = 0.1$ N/m, $Q_{\text{cl}} = 1.5$, $A_{\text{free}} = 3$ $\text{nm}_{\text{p}-0}$, $\tilde{A}_{\text{cl}} = 0.9$, and $\tilde{\omega}_{\text{drive}} = \tilde{\omega}_{\text{LMF}}$), $\alpha_{\text{Avg}\to\text{Peak}}$ is found to be 17. To examine the parameter dependence of $\alpha_{\text{Avg}\to\text{Peak}}$, calculations are performed by varying individual parameters while keeping all other parameters fixed. As shown in Fig. 7, the excitation frequencies—i.e., lower MinForce, peak, and f_0—produced nearly identical curves, although values at lower MinForce and peak frequencies were approximately 1.35 and 1.2 times higher than at f_0.

We first examined the dependence of E^* and R_{tip}, which has minimal impact on the average force. Here, $\alpha_{\text{Avg}\to\text{Peak}}$ increases with both E^* and R_{tip}. Typical AFM ranges for E^* and R_{tip} are 100–2000 Pa and 3–20 nm, respectively. Within these ranges, $\alpha_{\text{Avg}\to\text{Peak}}$ at the lower MinForce frequency ranges from 10–20 for E^*, and 16–20 for R_{tip}. For nonbiological samples with Young's modulus above 1 GPa, $\alpha_{\text{Avg}\to\text{Peak}}$ increases by a maximum of 50%. For k_{cl}, $\alpha_{\text{Avg}\to\text{Peak}}$ decreases as k_{cl} increases, while higher Q_{cl} and A_{free} led to an increase in $\alpha_{\text{Avg}\to\text{Peak}}$. In all cases, parameter variations of two–threefold result in only 20–30% errors. Since Q_{cl} differs significantly between solution and air, $\alpha_{\text{Avg}\to\text{Peak}}$ varies by a factor of 2–3. However, in ambient conditions, a cantilever with higher k_{cl} and larger A_{free} are required to prevent jump-to-contact, offsetting this variation. Thus, no significant difference in $\alpha_{\text{Avg}\to\text{Peak}}$ seems to be observed between these conditions. In practice, the setpoint is adjusted during measurement. While $\alpha_{\text{Avg}\to\text{Peak}}$ rapidly increases when $\tilde{A}_{\text{cl}}$ exceeds 0.98, the

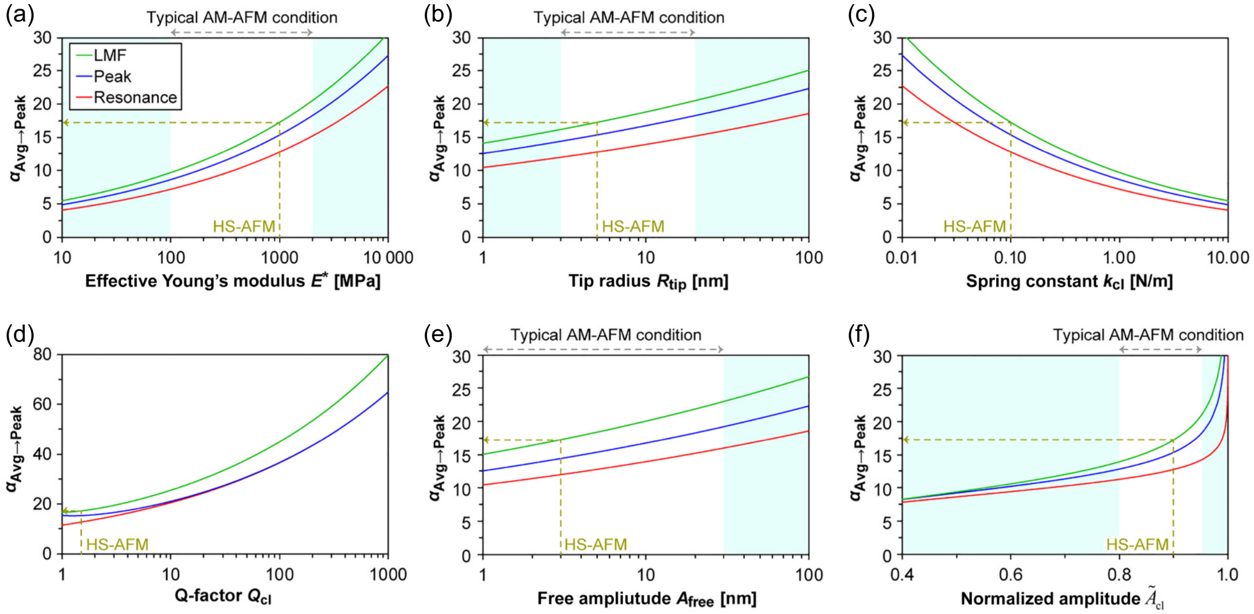

FIG. 7. (a)–(f) Ratio between the peak and average forces ($\alpha_{\mathrm{Avg}\to\mathrm{Peak}}$) as a function of (a) the reduced Young's modulus, (b) tip radius, (c) spring constant, (d) Q-factor, (e) free amplitude, and (f) normalized amplitude of the cantilever. Typical HS-AFM conditions are indicated by the gold arrows, while typical AM-AFM condition ranges are represented by the gray arrows.

variation remains within 30% in the typical range of 0.95 to 0.8.

In summary, peak force has a distinct functional form compared with average force. Although $\alpha_{\mathrm{Avg}\to\mathrm{Peak}}$ varies with measurement conditions, it is approximately 17 under typical HS-AFM conditions and generally ranges between 10 and 30. Since these parameters are independent, the curve shape remains consistent across conditions, allowing for easy adaptation by determining $\alpha_{\mathrm{Avg}\to\mathrm{Peak}}$.

IX. CONCLUSIONS

In this study, we succeeded in elucidating a previously unaddressed issue in that the force converted from the amplitude value in AM-AFM is substantially larger than the typical molecular binding forces. By analyzing the cantilever's equation of motion, we demonstrated that the conventional conversion formula, valid only for excitation at f_0, overestimates the force by up to five times. In contrast, our new method remains easy to use while providing more accurate estimates, even when exciting the cantilever at the resonance slope, where the imaging force is effectively reduced. This framework is applicable to both attractive and repulsive forces in ambient and liquid environments. While this study did not demonstrate under which conditions the average force or peak force would be dominant, we proposed a simple method for converting the average force to peak force. The insights and practical toolset provided here offer valuable support for researchers in materials and biomolecular studies using AM-AFM.

ACKNOWLEDGMENTS

We thank Dr. Steven J. McArthur at NanoLSI, Kanazawa University, for critical reading and improving the English language in this paper. This work was supported by PRESTO, Japan Science and Technology Agency (JST) [Grants No. JPMJPR20E3 and No. JPMJPR23J2 to K.U.] and KAKENHI, Japan Society for the Promotion of Science [Grants No. 21K04849 (to K.U.), No. 20H00327, and No. 24H00402 (to N.K.)].

K.U. constructed the theories and wrote the manuscript, K.K. supported the study, and N.K. supervised the study.

DATA AVAILABILITY

The data that support the findings of this study are available from the corresponding author upon reasonable request.

[1] Y. Martin, C. C. Williams, and H. K. Wickramasinghe, Atomic force microscope-force mapping and profiling on a sub 100 Å scale, J. Appl. Phys. **61**, 4723 (1987).

[2] R. Garcia and R. Perez, Dynamic atomic force microscopy methods, Surf. Sci. Rep. **47**, 197 (2002).

[3] B. Voigtländer, *Atomic Force Microscopy*, 2nd ed. (Springer, Berlin, 2019).

[4] R. Giridharagopal, L. Q. Flagg, J. S. Harrison, M. E. Ziffer, J. Onorato, C. K. Luscombe, and D. S. Ginger, Electrochemical strain microscopy probes morphology-induced variations in ion uptake and performance in organic electrochemical transistors, Nat. Mater. **16**, 737 (2017).

[5] A. F. Payam and A. Passian, Imaging beyond the surface region: Probing hidden materials via atomic force microscopy, Sci. Adv. **9**, eadg8292 (2023).

[6] V. V. Korolkov, A. Summerfield, A. Murphy, D. B. Amabilino, K. Watanabe, T. Taniguchi, and P. H. Beton, Ultrahigh resolution imaging of thin films and single strands of polythiophene using atomic force microscopy, Nat. Commun. **10**, 1537 (2019).

[7] S. Chiodini, J. Kerfoot, G. Venturi, S. Mignuzzi, E. M. Alexeev, B. T. Rosa, S. Tongay, T. Taniguchi, K. Watanabe, A. C. Ferrari, and A. Ambrosio, Moiré modulation of Van Der Waals potential in twisted hexagonal boron nitride, ACS Nano **16**, 7589 (2022).

[8] H. Söngen, R. Bechstein, and A. Kühnle, Quantitative atomic force microscopy, J. Phys. Condens. Matter **29**, 274001 (2017).

[9] S. Shi, D. Guo, and J. B. Luo, Imaging contrast and tip-sample interaction of non-contact amplitude modulation atomic force microscopy with Q-control, J. Phys. D: Appl. Phys. **50**, 415307 (2017).

[10] A. F. Payam, D. Martin-Jimenez, and R. Garcia, Force reconstruction from tapping mode force microscopy experiments, Nanotechnology **26**, 185706 (2015).

[11] J. Snijder, C. Uetrecht, R. J. Rose, R. Sanchez-Eugenia, G. A. Marti, J. Agirre, D. M. A. Guérin, G. J. L. Wuite, A. J. R. Heck, and W. H. Roos, Probing the biophysical interplay between a viral genome and its capsid, Nat. Chem. **5**, 502 (2013).

[12] Y. C. Lin, Y. R. Guo, A. Miyagi, J. Levring, R. MacKinnon, and S. Scheuring, Force-induced conformational changes in PIEZO1, Nature **573**, 230 (2019).

[13] N. Chiaruttini, L. Redondo-Morata, A. Colom, F. Humbert, M. Lenz, S. Scheuring, and A. Roux, Relaxation of loaded ESCRT-III spiral springs drives membrane deformation, Cell **163**, 866 (2015).

[14] R. Garcia, R. Magerle, and R. Perez, Nanoscale compositional mapping with gentle forces, Nat. Mater. **6**, 405 (2007).

[15] T. Ando, T. Uchihashi, and S. Scheuring, Filming biomolecular processes by high-speed atomic force microscopy, Chem. Rev. **114**, 3120 (2014).

[16] T. Fukui, T. Uchihashi, N. Sasaki, H. Watanabe, M. Takeuchi, and K. Sugiyasu, Direct observation and manipulation of supramolecular polymerization by high-speed atomic force microscopy, Angew. Chem., Int. Ed. **57**, 15465 (2018).

[17] C. Ganser and T. Uchihashi, Measuring mechanical properties with high-speed atomic force microscopy, Microscopy **73**, 14 (2024).

[18] A. P. Nievergelt, N. Banterle, S. H. Andany, P. Gonczy, and G. E. Fantner, High-speed photothermal off-resonance atomic force microscopy reveals assembly routes of centriolar scaffold protein SAS-6, Nat. Nanotechnol. **13**, 696 (2018).

[19] K. Umeda, S. J. McArthur, and N. Kodera, Spatiotemporal resolution in high-speed atomic force microscopy for studying biological macromolecules in action, Microscopy **72**, 151 (2023).

[20] N. Kodera, D. Noshiro, S. K. Dora, T. Mori, J. Habchi, D. Blocquel, A. Gruet, M. Dosnon, E. Salladini, C. Bignon, Y. Fujioka, T. Oda, N. N. Noda, M. Sato, M. Lotti, M. Mizuguchi, S. Longhi, and T. Ando, Structural and dynamics analysis of intrinsically disordered proteins by high-speed atomic force microscopy, Nat. Nanotechnol. **16**, 181 (2021).

[21] T. Ando, T. Uchihashi, and T. Fukuma, High-speed atomic force microscopy for nano-visualization of dynamic biomolecular processes, Prog. Surf. Sci. **83**, 337 (2008).

[22] A. P. Perrino and R. Garcia, How soft is a single protein? The stress-strain curve of antibody pentamers with 5 pN and 50 pm resolutions, Nanoscale **8**, 9151 (2016).

[23] M. Stark, R. W. Stark, W. M. Heckl, and R. Guckenberger, Inverting dynamic force microscopy: From signals to time-resolved interaction forces, Proc. Natl. Acad. Sci. U. S. A. **99**, 8473 (2002).

[24] A. Raman, X. Xu, C. Carrasco, P. J. de Pablo, and J. Gomez-Herrero, Unmasking imaging forces on soft biological samples in liquids when using dynamic atomic force microscopy: A case study on viral capsids, Biophys. J. **95**, 2520 (2008).

[25] L. Gross, F. Mohn, P. Liljeroth, J. Repp, F. J. Giessibl, and G. Meyer, Measuring the charge state of an adatom with noncontact atomic force microscopy, Science **324**, 1428 (2009).

[26] D. Platz, D. Forchheimer, E. A. Tholén, and D. B. Haviland, Interaction imaging with amplitude-dependence force spectroscopy, Nat. Commun. **4**, 1360 (2013).

[27] M. H. Lee and W. H. Jhe, General theory of amplitude-modulation atomic force microscopy, Phys. Rev. Lett. **97**, 036104 (2006).

[28] A. J. Katan, M. H. van Es, and T. H. Oosterkamp, Quantitative force versus distance measurements in amplitude modulation AFM: a novel force inversion technique, Nanotechnology **20**, 165703 (2009).

[29] H. Hölscher and U. D. Schwarz, Theory of amplitude modulation atomic force microscopy with and without Q-Control, Int. J. Non-Linear Mech. **42**, 608 (2007).

[30] J. Legleiter, M. Park, B. Cusick, and T. Kowalewski, Scanning probe acceleration microscopy (SPAM) in fluids: Mapping mechanical properties of surfaces at the nanoscale, Proc. Natl. Acad. Sci. U. S. A. **103**, 4813 (2006).

[31] C. Hutter, D. Platz, E. A. Tholen, T. H. Hansson, and D. B. Haviland, Reconstructing nonlinearities with intermodulation spectroscopy, Phys. Rev. Lett. **104**, 050801 (2010).

[32] A. San Paulo and R. Garcia, Tip-surface forces, amplitude, and energy dissipation in amplitude-modulation (tapping mode) force microscopy, Phys. Rev. B **64**, 193411 (2001).

[33] T. R. Rodriguez and R. Garcia, Theory of Q control in atomic force microscopy, Appl. Phys. Lett. **82**, 4821 (2003).

[34] H. Nakajima, Y. Kunioka, K. Nakano, K. Shimizu, M. Seto, and T. Ando, Scanning force microscopy of the interaction events between a single molecule of heavy meromyosin and actin, Biochem. Biophys. Res. Commun. **234**, 178 (1997).

[35] S. Uchimura, Y. Oguchi, M. Katsuki, T. Usui, H. Osada, J. Nikawa, S. Ishiwata, and E. Muto, Identification of a strong binding site for kinesin on the microtubule using mutant analysis of tubulin, EMBO J. **25**, 5932 (2006).

[36] T. Kowalewski and J. Legleiter, Imaging stability and average tip-sample force in tapping mode atomic force microscopy, J. Appl. Phys. **99**, 064903 (2006).

[37] J. Legleiter, The effect of drive frequency and set point amplitude on tapping forces in atomic force microscopy: simulation and experiment, Nanotechnology **20**, 245703 (2009).

[38] V. Vahdat and R. W. Carpick, Practical method to limit tip-sample contact stress and prevent wear in amplitude modulation atomic force microscopy, ACS Nano **7**, 9836 (2013).

[39] U. Dürig, Interaction sensing in dynamic force microscopy, New J. Phys. **2**, 5 (2000).

[40] T. R. Albrecht, P. Grütter, D. Horne, and D. Rugar, Frequency modulation detection using high-Q cantilevers for enhanced force microscope sensitivity, J. Appl. Phys. **69**, 668 (1991).

[41] A. San Paulo and R. Garcia, Unifying theory of tapping-mode atomic-force microscopy, Phys. Rev. B **66**, 041406 (2002).

[42] A. N. Round and M. J. Miles, Exploring the consequences of attractive and repulsive interaction regimes in tapping mode atomic force microscopy of DNA, Nanotechnology **15**, S176 (2004).

[43] B. A. Bircher, R. Krenger, and T. Braun, Influence of squeeze-film damping on higher-mode microcantilever vibrations in liquid, EPJ Tech. Instrum. **1**, 10 (2014).

[44] Asylum, MFP 3D User Guide, https://www.afmhelp.com/docs/manuals/mfp3dmanual.pdf (Accessed July 1, 2024).

[45] JPK, NanoWizard 3 User Manual, https://www.nanophys.kth.se/nanolab/afm/jpk/manuf-manuals/usermanual.4.2.pdf (Accessed July 1, 2024).

[46] Veeco, MultiMode SPM Instruction Manual, https://www.cigs.unimo.it/cigsdownloads/labs/afm2/manuali_letture/multimode_manual_revb.pdf (Accessed July 1, 2024).

[47] Park Systems, Web site, https://www.parksystems.com/jp/jp/park-spm-modes/91-standard-imaging-mode/2204-tapping-mode (Accessed July 1, 2024).

[48] Agilent Technologies, 5500 Scanning Probe Microscope User's Guide, https://afmhelp.com/docs/manuals/agilent_5500_user_manual_revB.pdf (Accessed July 1, 2024).

[49] K. Neupane, D. A. N. Foster, D. R. Dee, H. Yu, F. Wang, and M. T. Woodside, Direct observation of transition paths during the folding of proteins and nucleic acids, Science **352**, 239 (2016).

[50] F. Rico, A. Russek, L. González, H. Grubmüller, and S. Scheuring, Heterogeneous and rate-dependent streptavidin-biotin unbinding revealed by high-speed force spectroscopy and atomistic simulations, Proc. Natl. Acad. Sci. U. S. A. **116**, 6594 (2019).

[51] See Supplemental Material at http://link.aps.org/supplemental/10.1103/PhysRevApplied.23.034065, which includes Refs. [52–55], for additional theoretical considerations and further support of the derived theory.

[52] K. Umeda, K. Kobayashi, K. Matsushige, and H. Yamada, Direct actuation of cantilever in aqueous solutions by electrostatic force using high-frequency electric fields, Appl. Phys. Lett. **101**, 123112 (2012).

[53] H. Hölscher, Quantitative measurement of tip-sample interactions in amplitude modulation atomic force microscopy, Appl. Phys. Lett. **89**, 123109 (2006).

[54] S. Muthukumar and R. DesRoches, A Hertz contact model with non-linear damping for pounding simulation, Earthq. Eng. Struct. Dyn. **35**, 811 (2006).

[55] A. San Paulo and R. Garcia, Amplitude, deformation and phase shift in amplitude modulation atomic force microscopy: a numerical study for compliant materials, Surf. Sci. **471**, 71 (2001).

[56] D. Ebeling, H. Hölscher, and B. Anczykowski, Increasing the Q factor in the constant-excitation mode of frequency-modulation atomic force microscopy in liquid, Appl. Phys. Lett. **89**, 203511 (2006).

[57] V. G. Gisbert and R. Garcia, Accurate wide-modulus-range nanomechanical mapping of ultrathin interfaces with bimodal atomic force microscopy, ACS Nano **15**, 20574 (2021).

[58] E. K. Dimitriadis, F. Horkay, J. Maresca, B. Kachar, and R. S. Chadwick, Determination of elastic moduli of thin layers of soft material using the atomic force microscope, Biophys. J. **82**, 2798 (2002).

[59] M. Radmacher, M. Fritz, J. P. Cleveland, D. A. Walters, and P. K. Hansma, Imaging adhesion forces and elasticity of lysozyme adsorbed on mica with the atomic force microscope, Langmuir **10**, 3809 (1994).

[60] D. P. Kharakoz, Protein compressibility, dynamics, and pressure, Biophys. J. **79**, 511 (2000).

[61] H.-J. Butt, K. Graf, and M. Kappl, *Physics and Chemistry of Interfaces*, 2nd ed. (Wiley-VCH, Weinheim, Germany, 2006).

[62] J. L. Hutter and J. Bechhoefer, Calibration of atomic-force microscope tips, Rev. Sci. Instrum. **64**, 1868 (1993).

[63] J. E. Sader, J. N. Lu, and P. Mulvaney, Effect of cantilever geometry on the optical lever sensitivities and thermal noise method of the atomic force microscope, Rev. Sci. Instrum. **85**, 113702 (2014).

[64] R. Proksch, T. E. Schaffer, J. P. Cleveland, R. C. Callahan, and M. B. Viani, Finite optical spot size and position corrections in thermal spring constant calibration, Nanotechnology **15**, 1344 (2004).

[65] K. Umeda and N. Kodera, Guidelines for fast and nondestructive imaging in AM-AFM, arXiv:2411.16317 (2024).

[66] M. Prasad, M. Kopycinska, U. Rabe, and W. Arnold, Measurement of Young's modulus of clay minerals using atomic force acoustic microscopy, Geophys. Res. Lett. **29**, 13 (2002).

[67] G. H. Zeng, K. Dirscherl, and J. Garnaes, Toward accurate quantitative elasticity mapping of rigid nanomaterials by atomic force microscopy: effect of acquisition frequency, loading force, and tip geometry, Nanomaterials **8**, 616 (2018).